Journal of Biomedical Optics 7(3), 341–349 (July 2002)

Development and calibration of an automated Mueller matrix polarization imaging system

Justin S. Baba
Jung-Rae Chung
Aimee H. DeLaughter
Brent D. Cameron
Gerard L. Coté
Texas A&M University
Biomedical Engineering Program
College Station, Texas 77843-3120

Abstract. The high fatality rate associated with the late detection of skin cancer makes early detection crucial in preventing death. The current method for determining if a skin lesion is suspect to cancer is initially based on the patient's and physician's subjective observation of the skin lesion. Physicians use a set of parameters called the ABCD (asymmetry, border, color, diameter) rule to help facilitate diagnosis of potential cancerous lesions. Lesions that are suspicious then require a biopsy, which is a painful, invasive, and a time-consuming procedure. In an attempt to reduce the aforementioned undesirable elements currently associated with skin cancer diagnosis, a novel optical polarization-imaging system is described that has the potential to noninvasively detect cancerous lesions. The described system generates the full 16-element Mueller matrix in less than 70 s. The operation of the system was tested in transmission, specular reflection, and diffuse reflectance modes, using known samples, such as a horizontal linear polarizer, a mirror, and a diffuser plate. In addition, it was also used to image a benign lesion on a human subject. The results of the known samples are in good agreement with their theoretical values with an average accuracy of 97.96% and a standard deviation of 0.0084, using 16 polarization images. The system accuracy was further increased to 99.44% with a standard deviation of 0.005, when 36 images were used to generate the Mueller matrix. [DOI: 10.1117/1.1486248]

Keywords: Mueller matrix; skin cancer; polarization imaging; transmission; backscattering.

Paper JBO-TP-08 received Aug. 30, 2001; revised manuscript received Mar. 19, 2002; accepted for publication Apr. 1, 2002.

1 Introduction

One out of every seven Americans is afflicted with skin cancer in one of its various forms.[1] Skin cancer currently ranks as the seventh most common form of cancer in both Caucasian males and females.[2] In terms of the types, the three primary forms are basal cell carcinoma, squamous cell carcinoma, and melanoma. Of these, melanoma only accounts for approximately 5% of all skin cancers but is the most deadly form, accounting for approximately 75% of all skin cancer deaths.[2] Melanomas originate in the melanocytes which are the cells that produce the skin pigment known as melanin. These cells are located in the lower part of the epidermis and, therefore, may mask themselves as a common mole making detection difficult. Often melanoma-based lesions are left undiagnosed until they metastasize and affect other tissues and organs throughout the body. As such, early detection is paramount for the successful treatment of this disease with an average success rate of 95%.[1]

Currently the only available methods to diagnose suspected cancerous lesions are by visual inspection and the subsequent biopsy of the lesion. Using only visual inspection, nearly one-third of all melanomas are misdiagnosed and left untreated.[3] For those that do fall under the physician's suspicion through the use of the ABCD (asymmetry, border, color, diameter) rule, a biopsy is performed, requiring the surgical removal of the tissue for a microscopic histological examination that is subjective, invasive, expensive, and a time-consuming process. Therefore, there is a need for the development of an accurate and noninvasive skin cancer detection technique that is potentially automated and able to provide real-time results.

One such proposed technique uses a polarimetric optical approach to detect skin cancer by focusing on the changes in the optical properties as the stage of cancer progresses. These optical properties, in part, change due to uncontrolled cellular growth and division resulting in the disruption of the natural order of the tissue fibers as well as a variety of other factors.

The basis of polarimetry is well founded, beginning in the early 1800's when Biot developed the first documented polarimeter,[4] which found applications in the agricultural field of sugar production.[5–7] In the middle to late 1800's, Louis Pasteur advanced polarimetry into the field of monitoring bioprocesses, such as using polarimetry to identify and solve problems encountered during the fermentation processes of wine, beer, and vinegar,[8] which he identified as being caused by micro-organisms.[9] In 1976, Bickel et al. advanced polarimetry into the field of biomedical sensing when they de-

Brent D. Cameron is now with the Department of Bioengineering at the University of Toledo, OH.
Address all correspondence to Gerard L. Coté. E-mail: cote@tamu.edu

1083-3668/2002/$15.00 © 2002 SPIE

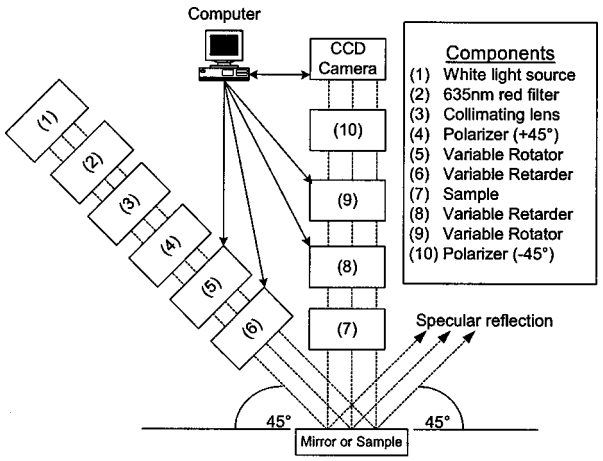

Fig. 1 Block diagram of the designed and implemented automated Mueller matrix polarization imaging system.

scribed a technique that measured the polarization effects of the scattered light from bacterial suspensions to yield useful information to characterize the samples.[10] In the ensuing decades, several groups have shown that a considerable amount of information can be obtained from polarization sensitive measurements such as the average particle size,[11] photon path length,[12] and particle shape[13–15] of the sample under investigation.[16] In addition, others have shown that polarization-based imaging measurements can provide an enhancement in superficial[17–19] structures to allow for subsurface imaging.[20] These aforementioned applications of polarimetry for biomedical imaging involve the use of Mueller–Stokes calculus to mathematically depict how a biological sample affects the polarization vector of an incident light beam, determined by either backscattered[9–12,21,22] or transmitted[23–25] light intensities from the sample.

The emphasis of this investigation is the development and demonstration of an automated electro-optical imaging system for measuring the full 16-element Mueller matrix (16-EMM) that overcomes most of the shortcomings of previously developed systems. The shortcomings of these manual and semiautomated systems include reproducibility problems, slow speeds leaving them subject to noise from motion artifact, and use of single point detection schemes,[18,20] which are impractical for *in vivo* imaging of lesions. Pezzaniti et al. have presented data for a mechanical transmission-based 16-EMM polarization imaging system. For their system, it took approximately 3 min to sequence through all of the measurements recorded by a 512×512 charge coupled device (CCD) detector.[19] Our group is the first to develop a fully operational, automated polarization imaging system with no moving parts, that works in both transmission and reflectance modes for the eventual use in biomedical imaging applications.

2 System Setup

The optical polarimetric imaging system, shown in Figure 1, consists of two branches, which contain the optics necessary to create the input and output polarization states required for deriving the 16-EMM. As depicted in Figure 1, the output beam from a white light source, component (1), (Navitar, Rochester, NY) passes through a red 633.8 nm filter, compo-

M_{11} =HH+HV+VH+VV	M_{12} =HH+HV-VH-VV	M_{13} =2PH+2PV-M_{11}	M_{14} =2RH+2RV-M_{11}
M_{21} =HH-HV+VH-VV	M_{22} =HH-HV-VH+VV	M_{23} =2PH-2PV-M_{21}	M_{24} =2RH-2RV-M_{21}
M_{31} =2HP+2VP-M_{11}	M_{32} =2HP-2VP-M_{12}	M_{33} =4PP-2PH-2PV-M_{31}	M_{34} =4RP-2RH-2RV-M_{31}
M_{41} =2HR+2VR-M_{11}	M_{42} =2HR-2VR-M_{12}	M_{43} =4PR-2PH-2PV-M_{41}	M_{44} =4RR-2RH-2RV-M_{41}

(a)

M_{11} =HH+HV+VH+VV	M_{12} =HH+HV-VH-VV	M_{13} =PH+PV-MH-MV	M_{14} =RH+RV-LH-LV
M_{21} =HH-HV+VH-VV	M_{22} =HH-HV-VH+VV	M_{23} =PH-PV-MH+MV	M_{24} =RH-RV-LH+LV
M_{31} =HP-HM+VP-VM	M_{32} =HP-HM-VP+VM	M_{33} =PP-PM-MP+MM	M_{34} =RP-RM-LP+LM
M_{41} =HR-HL+VR-VL	M_{42} =HR-HL-VR+VL	M_{43} =PR-PL-MR+ML	M_{44} =RR-RL-LR+LL

(b)

Fig. 2 Calculation of the 36-image Mueller matrix (a) using 16 polarization images and (b) using 36 polarization images. The notation is as follows: the first term represents the input polarization state while the second term represents the output polarization state. The states are defined as: H =horizontal, V=vertical, P=+45°, M=−45°, R=right circular, and L=left circular.

nent (2), (Thermo Oriel, Stratford, CT) then is collimated by a convex lens (f 38.1 mm), component (3), (Newport Corporation, Fountain Valley, CA) before being linearly polarized, oriented at $+45°$ (P state), by a Glan Thompson 100 000:1 polarizer (1 cm diam window), component (4), (Newport Corporation, Fountain Valley, CA). The ensuing P-state polarized beam then passes through an electro-optical variable polarization rotator (LPR-200-632, 2.1 cm diam window), component (5), and a variable retarder (LRC-200, 2.1 cm diam window), component (6), (Meadowlark Optics, Frederick, CO) that are used to produce the different input polarization states necessary for probing the sample, component (7). After probing the sample, the backscattered or transmitted light propagates through the detection optical train, components (8)–(10), which consist of the same components as in the input optical train but in reverse order, with the polarizer, component (10) set at $-45°$ (M state), before being imaged by a 14 bit (16 384 dynamic range), 20 μm pixel size, 509$\times$511, TE-cooled CCD camera (Apogee, Auburn, CA) fitted with a zoom lens (COSMICAR TV zoom lens, f 12.5–75 mm, 1.1.8 D; COSMICAR/PENTAX Precision Co., Tokyo, Japan). The samples used were air, an aluminum coated mirror, a Glan Thompson 100 000:1 polarizer (1 cm diam window), and an opal glass diffuser plate (Edmund Scientific Co., Barrington, NJ).

To achieve automation, all of the electro-optical components and the CCD camera are controlled and sequenced via a LabVIEW© 5.1 program. The program produces 2 kHz square waves with the appropriate output voltages used to control the electro-optic polarization rotators and variable retarders to achieve a given polarization state, before it sequences the camera to expose and save the image. The acquired images are manipulated via a MATLAB® 5.3 program which performs the calculations shown in Figures 2(a) and 2(b) used to generate the 16-EMM from either 16 or 36 polarization images.

Each branch of the system is mounted on a movable optical rail allowing for imaging measurements to be collected in either transmission, specular reflection, or diffuse reflectance modes depending on the difference in the angle between the two branches. The spacing between the components varied depending on the location of electric connectors and accessories. The distance of the sample from the light source was approximately 30 cm and of the sample from the camera was approximately 40 cm. For this paper, transmission mode data were collected with an angle, between the input and output arms of 180° and the specular reflection and diffuse reflection mode data were collected with an angle of 45°, with the difference being the alignment of the mirror to direct the specular reflection through the detection optics for the former case, and away from the detection optics in the later case. Figure 1 depicts the system setup to collect data in the diffuse reflection mode.

3 Theory

Polarized light can be completely described using the 4×1 Stokes vector, as demonstrated in Eq. (1).[26] In Eq. (1), S_0 is the total detected light intensity which corresponds to the addition of any of the orthogonal component intensities, while S_1 is the portion of the intensity that corresponds to the difference between the square of the linear horizontal and vertical polarization states, S_2 is the portion of the intensity that corresponds to the square of the difference between the linear $+45°(P)$ and $-45°(M)$ polarization states, and S_3 is the portion of the intensity that corresponds to the square of the difference between the right circular and left circular polarization states.[27] The Mueller matrix is a mathematical representation of the optical polarization properties of a given sample in which the Stokes vector of a probing light source can be combined with the Mueller matrix of the sample to determine the polarization state of the detected output beam. As a result, from Eq. (1), knowing the input light polarization state, $[S]_{\mathrm{IN}}$, and the detected light polarization state, $[S]_{\mathrm{OUT}}$, the sample 16-EMM, $[M]$, can be determined

$$\begin{bmatrix} S_0 \\ S_1 \\ S_2 \\ S_3 \end{bmatrix}_{\mathrm{OUT}} = \begin{bmatrix} M_{11} & M_{12} & M_{13} & M_{14} \\ M_{21} & M_{22} & M_{23} & M_{24} \\ M_{31} & M_{32} & M_{33} & M_{34} \\ M_{41} & M_{42} & M_{43} & M_{44} \end{bmatrix} \begin{bmatrix} S_0 \\ S_1 \\ S_2 \\ S_3 \end{bmatrix}_{\mathrm{IN}} . \quad (1)$$

For a given sample, this can be accomplished with a minimum of 16 polarization images, as depicted in Figure 2(a).[28] More images may be used, such as 36 polarization images, depicted in Figure 2(b), or 49 polarization images.[29] Using more than 16 images has inherent benefits, which are discussed later. The 16-image derivation, in Figure 2(a), can be achieved by the simplification of the 36-image derivation, in Figure 2(b), by applying polarization relationships (e.g., $H+V=P+M=R+L$).[30]

Since biomedical imaging applications include measurements in transmission, and diffuse reflectance modes, we modeled and tested our system for each of these modalities and also for specular reflection mode. The theory for the results we present is well developed and documented in literature.[31,32]

4 Calibration

The electro-optical elements present in the system were first calibrated by a nulling technique involving the use of an input (4) and output (10) polarizer oriented with their transmission axes at 90° with respect to each other. More specifically, each component was calibrated by adjusting the voltage supplied to it from a function generator until the desired input and output polarization states of H, V, P, and M were obtained by the detection of a minimum intensity by the camera. The calibration was done sequentially beginning with the output rotator, component (9). The required voltages to obtain the necessary degree of rotation from the output rotator for each of the desired polarization states, was determined by changing the state of the input polarizer, leaving the output polarizer state constant (M state), and adjusting the voltage output until the desired intensity was captured by the camera. Next, the input polarization rotator, component (5), was then similarly calibrated. For the input electro-optical retarder, component (6), both the input and output polarization states were fixated, input at P state and output at M state, and an L state circular polarizer was used as a sample while the retarder voltage was adjusted to give the desired intensity values for each input polarization state. Finally, the output electro-optical retarder, component (8), was calibrated by setting the input arm polar-

ization to the appropriate state, and then adjusting the voltage to the retarder to give the corresponding intensity values. For example, for the case *H* input, *R* output, the input arm was set to produce an *H* state, and the amplitude of the 2 kHz square wave to the retarder was adjusted for quarter-wave retardance. The acquired control voltages were then stored into a LabVIEW© 5.1 control program and sent to the system components via a digital/analog board. All of the output control voltages were conditioned via low pass analog filters[33] to reduce artifacts present in the output square waves.

To test our system, we used a horizontal linear polarizer as the sample. For all matrices, we collected 16 and 36 polarization state images, computed the mean intensity values for the known minimum intensity images and subtracted this minimum from all images. After base line correction, all computed Mueller matrix images were normalized via division by the M_{11} image.

5 Results and Discussion

Before collecting any sample data, the precision of the described system was tested after calibration. This was accomplished by determining the system variability between ten successive runs. Since the two post calibration precision results were similar, only the results obtained after calibrating the system for diffuse reflectance mode are presented. These results indicate an accuracy within 97.96% and a standard deviation of 0.0084 using 16 polarization images and 99.44% accuracy with a standard deviation of 0.005 when 36 images were used to generate the Mueller matrix.

In order to determine the average values depicted in (b) and (c) of the figures, the black background border from the optical holders was removed. The area used for the calculation was roughly 1 cm in diameter and had dimensions of 360×360 pixels for all samples, except for the skin where the extracted area was 130×130 pixels to encompass primarily the information around the mole. This is illustrated by the white box in the M_{11} element of (d) in the figures. Note that the Mueller matrix images depicted in (a) of the figures included the border but were scaled by the M_{11} element.

5.1 Transmission Mode

For the case of transmission, the system was aligned and calibrated to test for the expected theoretical values.

5.1.1 *Case: No Sample (Air)*

The raw intensity values (arbitrary units) ranged from a 735 minimum to an 11 683 maximum. As theoretically expected, the experimentally measured Mueller matrix for the case of no sample is in the form of the identity matrix for each reconstruction case, as depicted in Figures 3(b) and 3(c). The maximum elemental error was 1.79% for the 36-image derived Mueller matrix, and 3.53% for the 16-image derived matrix.

5.1.2 *Case: Horizontal Polarizer Sample*

The raw intensity values detected ranged from a 646.2 minimum to a 9686.5 maximum. As theoretically expected for the case of a horizontal polarizer sample, the experimentally measured Mueller matrix is of the form of a horizontal polarizer for each reconstruction case, as depicted in Figures 4(b) and 4(c). The maximum elemental error was 2.02% for the 36-image derived Mueller matrix and 3.13% for the 16-image derived matrix.

5.2 Specular Reflection Mode

To acquire specular reflection measurements, a mirror was installed between the realigned input and output branches such that the reflection from the mirror was directed through the detection-optics branch. The system was then calibrated and tested for specular reflection mode.

5.2.1 *Case: Mirror Sample*

The raw intensity values detected ranged from a 671.2 minimum to a 9365.5 maximum. As theoretically expected for the case of a mirror sample, the experimentally measured Mueller matrix for each reconstruction case is in the form of the reflection identity matrix, as depicted in Figures 5(b) and 5(c). The maximum elemental error was 1.48% for the 36-image derived Mueller matrix and 2.80% for the 16-image derived matrix.

5.2.2 *Case: Horizontal Polarizer Sample*

The raw intensity values detected ranged from a 646.0 minimum to a 8483.1 maximum. As theoretically expected, for the case of a horizontal polarizer sample between the mirror and the output arm of the system, the experimentally measured Mueller matrix for each reconstruction case is in the form of a horizontal polarizer sample matrix for both depicted cases in Figures 6(b) and 6(c). For this case, the maximum elemental error was 3.74% for the 36-image derived Mueller matrix and 6.00% for the 16-image derived matrix.

5.3 Diffuse Reflectance Mode

To test the system in diffuse reflectance mode, the angle of the mirror was adjusted to direct the specular reflection from the mirror away from the detection-optics branch (see Figure 1), thus, allowing for backscattering measurements only. Measurements for the following cases were collected.

5.3.1 *Case: Diffuser Plate Sample*

The raw intensity values detected ranged from a 1253.4 minimum to a 1346.8 maximum. As expected from theory, the experimentally measured Mueller matrix for this case is in the form of a diffuser plate sample matrix regardless of the reconstruction method, as depicted in Figures 7(b) and 7(c). The maximum elemental error for the 36-image and 16-image derived Mueller matrix is 1.25% and 4.61%, respectively.

5.3.2 *Case: Human Skin*

The raw intensity values detected ranged from a 4954 minimum to an 11 603 maximum. As predicted from the theory, human skin does not completely depolarize the probing light beam but exhibits birefringence in addition to reflectance as indicated by the values in the diagonal and off diagonal elements in comparison to those values for complete depolarization [Figure 7(a)] and complete mirror reflection [Figure 5(a)]. Also, as expected from the work of Jacques et al.,[17–19]

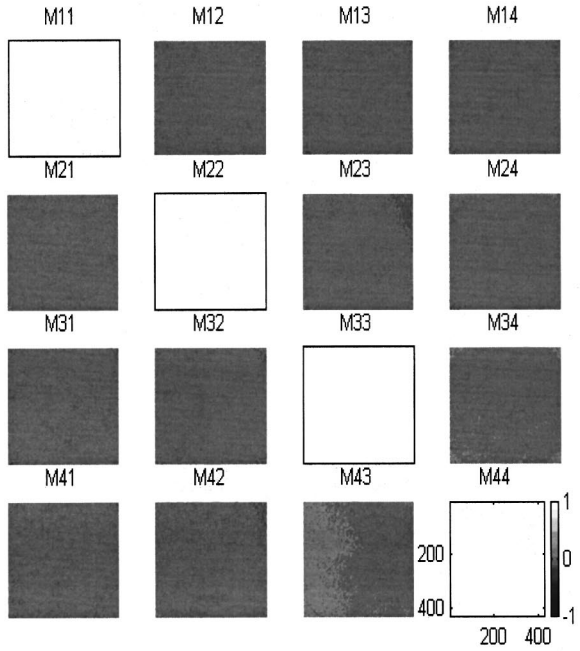

Experimental (Air 16-images)			
1.0000	0.0059	-0.0098	-0.0148
0.0094	0.9947	-0.0271	-0.0184
-0.0080	-0.0275	1.0091	0.0251
-0.0195	-0.0303	0.0353	0.9925

(b)

Experimental (Air 36-images)			
1.0000	0.0059	0.0069	-0.0102
0.0094	0.9947	-0.0179	-0.0117
0.0138	-0.0135	1.0030	-0.0127
-0.0027	-0.0033	-0.0017	0.9985

(c)

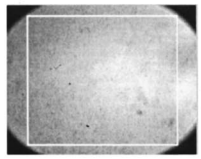

(d)

Fig. 3 16-EMM without a sample (for air), collected in transmission mode. (a) These images are derived from the original 36 images as shown in Figure 2(b). (b) Mean values for the 16-EMM using 16 images as shown in Figure 2(a). (c) Mean values for the 16-EMM using 36 images as shown in Figure 2(b). (d) Raw un-normalized image of $M_{\|}$ element. The white box indicates the extracted area used to generate the numerical results presented in (a) and in (b).

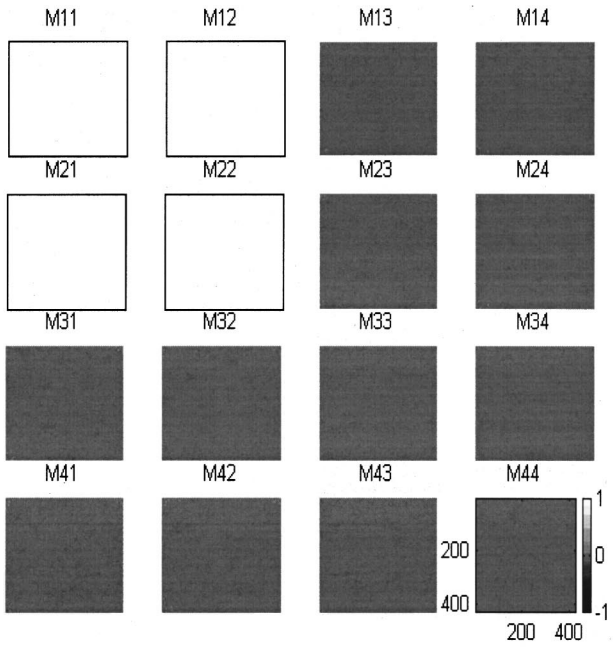

Experimental (M 16-images)			
1.0000	1.0002	0.0218	0.0281
1.0001	1.0001	0.0217	0.0280
0.0313	0.0312	-0.0207	-0.0209
0.0303	0.0302	-0.0207	-0.0210

(b)

Experimental (M 36-images)			
1.0000	1.0002	0.0125	0.0124
1.0001	1.0001	0.0125	0.0125
0.0130	0.0130	-0.0101	-0.0112
0.0202	0.0202	-0.0081	-0.0126

(c)

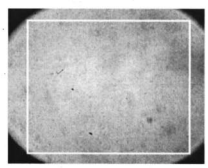

(d)

Fig. 4 16-EMM for a horizontal polarizer sample, collected in transmission mode. (a) These images are derived from the original 36 images as shown in Figure 2(b). (b) Mean values for the 16-EMM using 16 images as shown in Figure 2(a). (c) Mean values for the 16-EMM using 36 images as shown in Figure 2(b). (d) Raw un-normalized image of $M_{\|}$ element. The white box indicates the extracted area used to generate the numerical results presented in (a) and in (b).

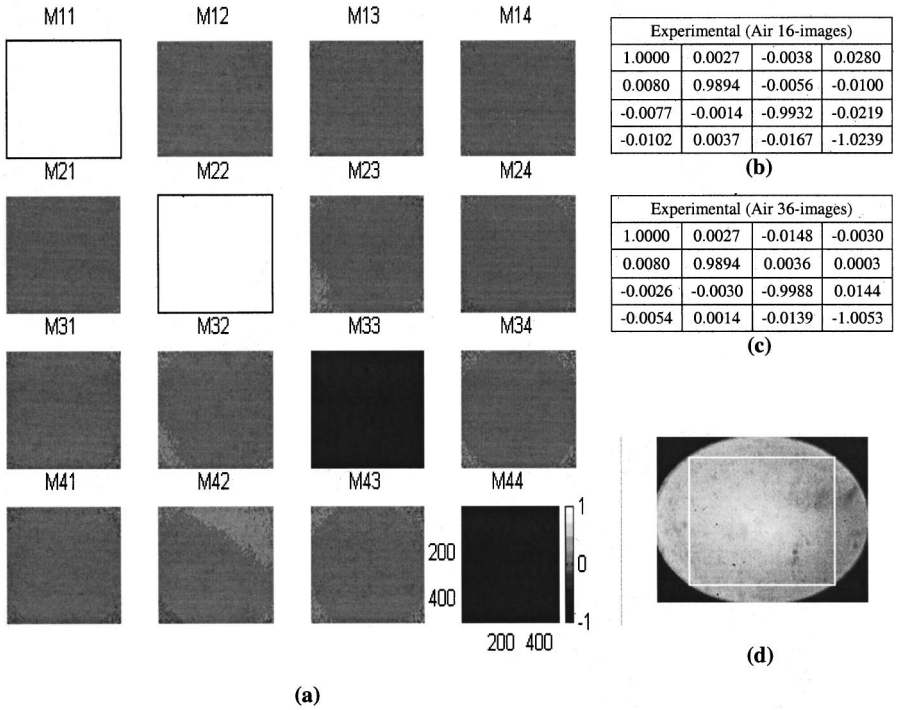

Fig. 5 16-EMM for a mirror sample, collected in specular reflection mode. (a) These images are derived from the original 36 images as shown in Figure 2(b). (b) Mean values for the 16-EMM using 16 images as shown in Figure 2(a). (c) Mean values for the 16-EMM using 36 images as shown in Figure 2(b). (d) Raw un-normalized image of $M_{\|}$ element. The white box indicates the extracted area used to generate the numerical results presented in (a) and in (b).

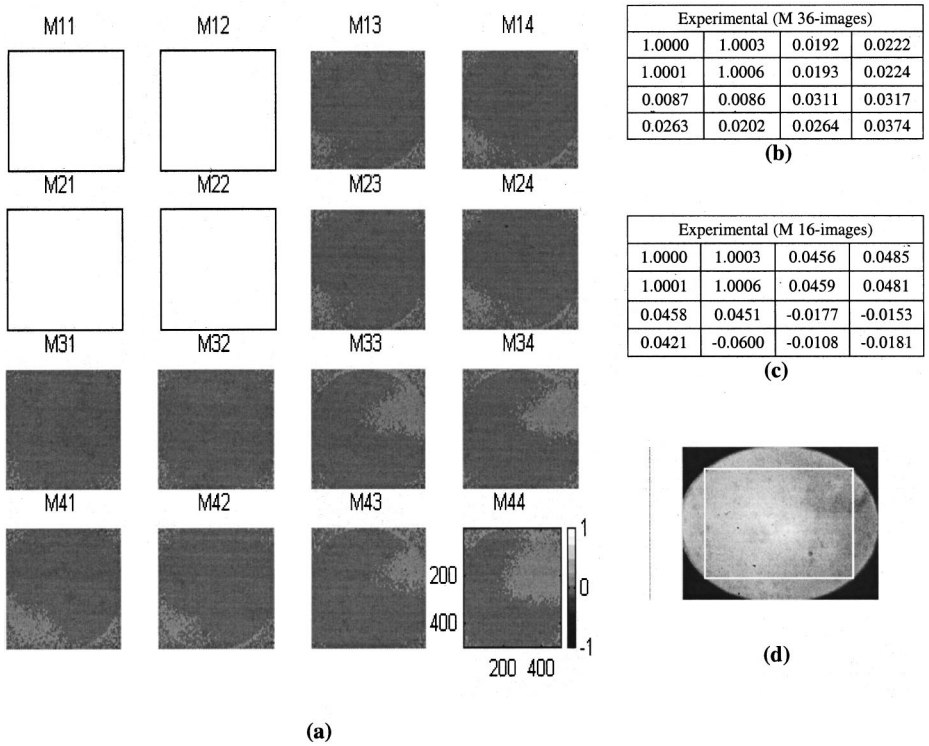

Fig. 6 16-EMM for a horizontal polarizer sample, collected in specular reflection mode. (a) These images are derived from the original 36 images as shown in Figure 2(b). (b) Mean values for the 16-EMM using 16 images as shown in Figure 2(a). (c) Mean values for the 16-EMM using 36 images as shown in Figure 2(b). (d) Raw un-normalized image of $M_{\|}$ element. The white box indicates the extracted area used to generate the numerical results presented in (a) and in (b).

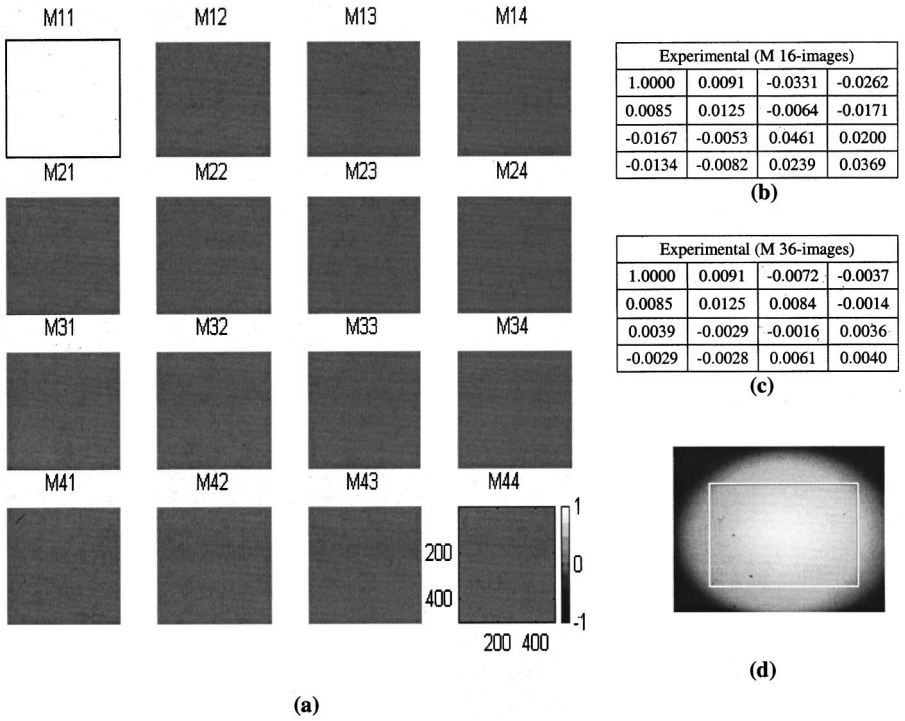

Fig. 7 Normalized 16-EMM for a diffuser plate sample collected in diffuse reflectance mode. (a) These images are derived from the original 36 images as shown in Figure 2(b). (b) Mean values for the 16-EMM using 16 images as shown in Figure 2(a). (c) Mean values for the 16-EMM using 36 images as shown in Figure 2(b). (d) Raw un-normalized image of $M_{\|}$ element. The white box indicates the extracted area used to generate the numerical results presented in (a) and in (b).

the birthmark that shows up as a black dot in the M_{11} element of Figure 8(a), disappears in the M_{12} and M_{21} cases, which are the crossed horizontal and vertical linear polarization cases. This subtraction of pigmentation from matrix elements, other than for elements M_{11} and M_{22}, which are the addition of the orthogonal horizontal and vertical linear polarization cases, confirms that polarization imaging can be used to eliminate pigmentation aliasing and allows the observation of the underlying tissue structure. In addition, the differences in the details of the underlying tissue structure between the elements other than M_{11} and M_{22}, indicate that the retention of polarization information is also dependent on the system input and output polarization states.

6 Conclusion

The presented results establish the ability of the described automated Mueller matrix imaging system to precisely measure within a 97% accuracy the 16-EMM of a sample in either transmission, specular reflection, or backscattering modes. In the current configuration, it is clear that using 36 versus 16 polarization images in the Mueller matrix reconstruction process is a trade off between maximizing accuracy (a benefit of using an overdetermined system) and acquisition time. Depending on the reconstruction process, it takes approximately 70 or 150 s to reconstruct the 16-EMM using either the 16 or 36 polarization images, respectively, however, it should be noted that these times are not a direct reflection of the speed of either the electro-optic components or CCD camera. The current organization of our LabVIEW program is one of the reasons for the measurement delay, which will be optimized in the future.

The maximum sample calibration matrix element error of 6.00% and 3.74%, for 16 and 36 polarization images respectively, can be attributed, in part, to the 10.5 nm pass band width of the 633 nm red bandpass filter in front of the white light source. This lack of spectral purity in the probing light beam has the effect of increasing the retardation errors, which are extremely wavelength dependent, therefore, resulting in noticeable errors in the circular polarization containing matrix elements. Going to an incoherent, coherence scrambled laser source, or using a narrower pass band filter could help compensate for this error.

Finally, the potential of the developed system for the detection of superficial cancerous lesions lies in its ability to remove pigmentation effects and to reject deeply backscattered light at different depths, based on the incident and backscattered polarizations within the tissue. These effects often mask the underlying superficial structures in white light tissue imaging. In addition, the ability to fully characterize the polarization properties of the sample under investigation can provide useful information in terms of the morphological structure differences present between normal and cancerous tissue. These changes can be used to help characterize and distinguish between tissue types. Furthermore, the ability to acquire such measurements in a minimal time frame gives promise for the future application of such a system to differ-

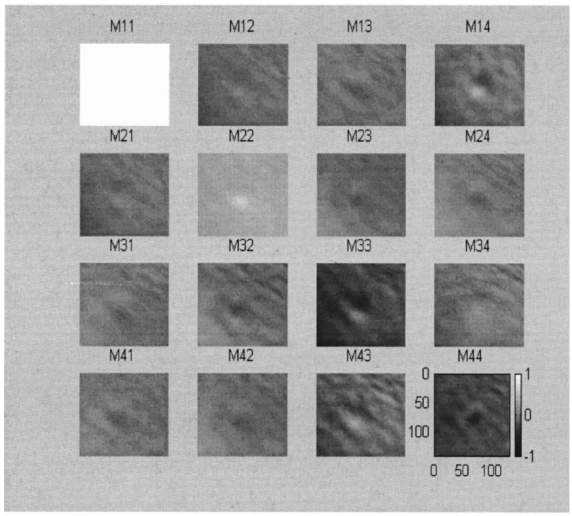

(a)

Experimental (M 36-images)			
1.0000	-0.0508	0.0086	-0.0021
-0.0473	0.3649	-0.0520	0.0401
-0.0006	-0.0555	-0.3649	0.0078
0.0043	-0.0145	-0.0846	-0.2915

(b)

Experimental (M 16-images)			
1.0000	-0.0508	-0.0009	-0.0402
-0.0473	0.3649	-0.0273	0.0657
0.0013	-0.0247	-0.3545	0.0159
0.0012	0.0155	-0.0284	-0.3088

(c)

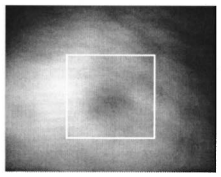

(d)

Fig. 8 16-element Mueller matrix collected from the normal skin of a black African subject. (a) These images are derived from the original 36 images as shown in Figure 2(b). Notice the birthmark pigmentation that shows up in the M_{11} and M_{22} elements, but is nonexistent in the other matrix elements. (b) Mean values for the 16-EMM using 16 images as shown in Figure 2(a). (c) Mean values for the 16-EMM using 36 images as shown in Figure 2(b). (d) Raw un-normalized image of $M_{\|}$ element. The total image shown was used to generate the numerical results presented in (a) and in (b).

entiate between normal, benign, and cancerous tissue. Future studies will be directed at exploring the angular dependence of such measurements and in the development of algorithms to aid in the characterization and differentiation process.

References

1. *What You Need to Know About Skin Cancer*, NIH-National Cancer Institute, NIH Publication No. 95-1564 (1995).
2. *Cancer: Rates and Risks*, NIH-National Cancer Institute, NIH Publication No. 96-691 (1996).
3. *The Melanoma Letter*, The Skin Cancer Foundation, New York (2001).
4. J. McMurry, *Organic Chemistry*, 3rd ed., Brooks/Cole, Pacific Grove, CA (1992).
5. B. E. R. Newlands, *Sugar*, Spon & Chamberlain, New York (1909).
6. C. A. Browne and F. W. Zerban, *Physical and Chemical Methods of Sugar Analysis*, 3rd ed., Wiley, New York (1941).
7. G. L. Spencer, *A Handbook for Cane-Sugar Manufacturers*, 6th ed., Wiley, New York (1917).
8. M. A. Fox and J. K. Whitesell, *Organic Chemistry*, 2nd ed., Jones and Barlett, Sudbury, MA (1997).
9. D. S. Eisenbergh and D. M. Crothers, *Physical Chemistry with Applications to the Life Sciences*, Benjamin/Cummings, Menlo Park, CA (1979).
10. W. S. Bickel, J. F. Davidson, D. R. Huffman, and R. Kilkson, ''Application of polarization effects in light scattering: A new biophysical tool,'' *Proc. Natl. Acad. Sci. U.S.A.* **73**, 486–490 (1976).
11. K. Sokolov, R. Drezek, K. Gossage, and R. Richards-Kortum, ''Reflectance spectroscopy with polarized light: Is it sensitive to cellular and nuclear morphology,'' *Opt. Express* **5**, 302–307 (1999).
12. M. Dogariu and T. Asakura, ''Photon pathlength distribution from polarized backscattering in random media,'' *Opt. Eng.* **35**, 2234–2239 (1996).
13. B. D. Cameron, M. J. Rakovic, M. Mehrubeoglu, G. W. Kattawar, S. Rastegar, L. V. Wang, and G. L. Coté, ''Measurement and calculation of the two-dimensional backscattering Mueller matrix of a turbid medium,'' *Opt. Lett.* **23**, 485–487 (1998).
14. B. D. Cameron, M. J. Rakovic, M. Mehrubeoglu, G. W. Kattawar, S. Rastegar, L. V. Wang, and G. L. Coté, ''Measurement and calculation of the two-dimensional backscattering Mueller matrix of a turbid medium,'' *Opt. Lett.* **23**, 1630 (1998).
15. M. J. Rakovic, G. W. Kattawar, M. Mehrubeoglu, B. D. Cameron, S. Rastegar, L. V. Wang, and G. L. Coté, ''Light backscattering polarization patterns from turbid media: Theory and experiment,'' *Appl. Opt.* **38**, 3399–3408 (1999).
16. A. H. Hielscher, J. R. Mourant, and I. J. Bigio, ''Influence of particle size and concentration on the diffuse backscattering of polarized light from tissue phantoms and biological cell suspensions,'' *Appl. Opt.* **36**, 125–135 (1997).
17. S. L. Jacques, M. Ostemeyer, L. V. Wang, and D. Stephens, ''Polarized light transmission through skin using video reflectometry: toward optical tomography of superficial tissue layers,'' *Proc. SPIE* **2671**, 199–210 (1996).
18. S. L. Jacques and K. Lee, ''Imaging tissues with a polarized light video camera,'' *Proc. SPIE* **3863**, 68–74 (1999).
19. S. L. Jacques and R. J. Ramella-Roman, ''Propagation of polarized light beams through biological tissues,'' *Proc. SPIE* **3914**, 345–352 (2000).
20. S. G. Demos and R. R. Alfano, ''Optical polarization imaging,'' *Appl. Opt.* **36**, 150–155 (1997).
21. A. H. Hielscher, A. A. Eick, J. R. Mourant, D. Shen, J. P. Freyer, and I. J. Bigio, ''Diffuse backscattering Mueller matrices of highly scattering media,'' *Opt. Express* **1**, 441–453 (1997).
22. F. Delplancke, ''Automated high-speed Mueller matrix scatterometer,'' *Appl. Opt.* **36**, 5388–5395 (1997).
23. J. M. Bueno, ''Polarimetry using liquid-crystal variable retarders: Theory and calibration,'' *J. Opt. A, Pure Appl. Opt.* **2**, 216–222 (2000).
24. J. L. Pezzaniti and R. A. Chipman, ''Mueller matrix imaging polarimetry,'' *Opt. Eng.* **34**, 1558–1568 (1995).
25. M. Mujat and A. Dogariu, ''Real-time measurement of the polarization transfer function,'' *Appl. Opt.* **40**, 34–44 (2001).
26. E. Hecht, *Optics*, 3rd ed., pp. 322–323, 366–367, 370, Addison Wesley Longman, Reading, MA (1998).
27. D. S. Kilger, J. W. Lewis, and C. Einterz Randall, *Polarized Light in Optics and Spectroscopy*, p. 77, Academic, San Diego, CA (1990).
28. G. Yao and L.-H. Wang, ''Two-dimensional depth-resolved Mueller matrix characterization of biological tissue by optical coherence tomography,'' *Opt. Lett.* **24**(8), 537–539 (1999).
29. W. S. Bickel and W. M. Bailey, ''Stokes vectors, Mueller matrices,

and polarized scattering,'' *Am. J. Phys.* **53**, 468–478 (1985).
30. B. D. Cameron, *The Application of Polarized Light to Biomedical Diagnostics and Monitoring*, PhD dissertation, Texas A&M University, College Station, TX (2000).
31. H. C. Van de Hulst, *Light Scattering by Small Particles*, Dover, New York (1981).
32. C. F. Bohren and D. R. Huffman, *Absorption and Scattering of Light by Small Particles*, Wiley, New York (1983).
33. J. W. Nilsson and S. A. Riedel, *Electric Circuits*, 5th ed., Addison-Wesley, Reading, MA (1996).